

# Cosmic-ray positron fraction measurement from 1 to 30 GeV with AMS-01

The AMS-01 Collaboration

## Abstract

A measurement of the cosmic ray positron fraction  $e^+/(e^+ + e^-)$  in the energy range of 1–30 GeV is presented. The measurement is based on data taken by the AMS-01 experiment during its 10 day Space Shuttle flight in June 1998. A proton background suppression on the order of  $10^6$  is reached by identifying converted bremsstrahlung photons emitted from positrons.

Submitted to *Phys. Lett. B*

# 1 Introduction

Over the past decades cosmic ray physics has joined astronomy as a means to gather information about the surrounding universe. Of the few particles that are stable and thus able to cross vast interstellar distances, electrons and positrons are of particular interest.

Electrons are believed to be accelerated in shock waves following supernova explosions. Their spectrum is subsequently altered by inverse Compton scattering off cosmic microwave background photons, synchrotron radiation due to the galactic magnetic field, bremsstrahlung processes in the interstellar medium and modulation in the solar magnetosphere. Thus they serve as an important probe of cosmic ray propagation models. On the other hand, positrons are produced secondarily in the decay cascades of  $\pi^+$ , which are created in hadronic interactions of cosmic ray protons with the interstellar medium. This yields an  $e^+/e^-$  ratio of roughly 10 %.

In addition to these classical sources, positrons may also originate from more exotic ones. Among the most important unsolved questions in modern cosmology is the nature of dark matter. Based on observations of the cosmic microwave background, supernovae of type IA and galaxy clustering, among others, the standard model of cosmology now contains a density of non-luminous matter exceeding that of baryonic matter by almost a factor of five [1]. The most promising candidate for dark matter is a stable weakly interacting massive particle predicted by certain supersymmetric extensions to the standard model of particle physics [2] and called the neutralino,  $\chi$ . Positrons and electrons will then be created in equal numbers as stable decay products of particles stemming from  $\chi$ - $\chi$  annihilations, for instance in the galactic halo. Such a process would constitute a primary source of positrons. Therefore, a measurement of the positron fraction is also motivated by the prospect of indirect dark matter detection, especially if combined with other sources of information, such as antiprotons, diffuse  $\gamma$ -rays or, more challenging, antideuterons.

## 2 The AMS-01 experiment

As a predecessor to the Alpha Magnetic Spectrometer AMS-02, which is to be operated on the International Space Station (ISS) for at least 3 years, the AMS-01 experiment was flown on the Space Shuttle *Discovery* from June 2nd to 12th, 1998.

The AMS-01 experiment consisted of a cylindrical permanent magnet with a bending power of  $0.14 \text{ Tm}^2$  and an acceptance of  $0.82 \text{ m}^2\text{sr}$ . The magnet bore was covered at each of the upper and lower ends with two orthogonal layers of scintillator paddles, forming the time of flight system (TOF). This provided a fast trigger signal as well as a measurement of velocity and charge number. The silicon tracking device consisted of six layers of double-sided silicon strip detectors mounted inside the magnet volume. Charged particle trajectories were reconstructed with an accuracy of better than  $20 \mu\text{m}$  in the bending coordinate. The momentum resolution at  $10 \text{ GeV}/c$  was about 10 % for singly charged particles. The inner magnet surface was lined with the scintillator panels of the anticoincidence system serving as a veto counter against particles traversing the magnet wall. Velocity measurements were augmented with a two-layered aerogel Čerenkov threshold counter (ATC) mounted underneath the lowest TOF layer, allowing  $e^+/p$  discrimination below  $3 \text{ GeV}/c$ . A low energy particle shield covered the experiment to absorb particles below  $5 \text{ MeV}$ , while a multi-layer insulation blanket served as a protection against space debris and solar radiation. The radiation thickness of all materials above the tracking device sums up to 18.2 % of a radiation length. Below the tracking device, not including the Space Shuttle, the material sums up to 19.1 % of a radiation length. A detailed description of the experiment is given in [3]. Orbiting with an inclination of  $\pm 50.7^\circ$  at altitudes between 320 and 390 km, AMS-01 recorded  $10^8$  events in 184 hours. During 4 days of the flight, the Space Shuttle was

docked to the Mir space station. Before and after docking, the Shuttle's yaw axis (AMS z-axis) was kept pointing at  $0^\circ$ ,  $20^\circ$ ,  $30^\circ$ ,  $45^\circ$  and  $180^\circ$  with respect to the zenith for several hours each. During docking its pointing varied continuously between  $40^\circ$  and  $145^\circ$ .

### 3 Conversion of bremsstrahlung photons

The main challenge of cosmic ray positron measurements is the suppression of the vast proton background. As is known from previous measurements [3, 4], the flux of cosmic ray protons exceeds that of positrons by a factor of  $10^4$  in the momentum range of 1–50 GeV/c. Hence, in order to keep the proton contamination of positron samples below 1 %, a proton rejection of  $10^6$  has to be reached. Since the ATC subdetector of AMS-01 provided a sufficient single track proton rejection only for energies below 3 GeV, a different approach has been chosen for this analysis. It relies on the identification of bremsstrahlung emission through photoconversion. Due to the inverse quadratic dependence on the particle mass of the cross section, bremsstrahlung emission is suppressed by a factor of more than  $3 \cdot 10^6$  for protons with respect to positrons.

Figure 1 shows the principle of a converted bremsstrahlung event signature. A primary positron enters the detector volume from above and emits a bremsstrahlung photon in the first TOF scintillator layer. The photon then converts into an electron-positron pair in the second TOF layer. Because of the low fraction of momentum which is typically carried away by the photon, the secondary particles have lower momenta than the primary. Therefore, in the bending plane projection, the secondaries tend to form the left and right tracks, while the primary remains in the middle.

Both bremsstrahlung and photon conversion are closely related electromagnetic processes whose energy and angular distributions can be calculated with the Bethe-Heitler formalism. In the relativistic limit, the angles of photon emission as well as the opening angles of pair production show distributions with a most probable value of  $\theta_0 \approx 1/\gamma$ ,  $\gamma$  being the Lorentz factor of the emitting particle or the electron-positron pair, respectively. In the GeV energy range, these values fall below the accuracy limit of the track reconstruction induced by multiple scattering, and thus are practically equal to zero.

The dominant backgrounds are caused by electrons with misreconstructed momentum sign and by protons undergoing hadronic reactions in the material distribution of the experiment. In the latter case, mesons are produced that mimic the 3-track signature of converted bremsstrahlung events. For example, in the reaction  $pN \rightarrow pN\pi^+\pi^- + X$ , where  $X$  are additional undetected particles, the charged pions can be misidentified as an electron-positron pair. Besides this, neutral pions produced in reactions of the type  $pN \rightarrow pN\pi^0 + X$  decay into two photons, one of which may escape undetected. If the remaining photon converts, the conversion pair will form a 3-track event together with the primary proton. However, the invariant masses of the mesons and the primary proton and photon are typically at the scale of the pion mass, leading to significantly larger emission angles.

### 4 Event reconstruction

In order to gain the highest possible selection efficiency, it is mandatory to apply sophisticated track and vertex finding algorithms which are particularly customized for the converted bremsstrahlung event signature [5]. To account for the asymmetric geometry of the detector along its z-axis, the analysis is performed separately for particles traversing the detector top-down (*downward*) and bottom-up (*upward*).

## 4.1 Preselection

As a first step, the hits in the silicon strip detectors of the tracker are projected into the bending plane for clustering. For further analysis, a minimum of 8 tracker clusters are required. Events are selected in which at least two of the six layers of silicon detectors signaled exactly three clusters (*triplets*).

## 4.2 Track finding

Since particle tracks diverge in the magnetic field, the triplets are required to have increasing cluster to cluster distances along the z-axis in the flight direction. Assuming that three particles have traversed the tracker, in events with three or more triplets the clusters in the triplets can be directly assigned to a left, a middle and a right track of minimum length. Starting with these track seeds, further clusters on the other layers are gradually added to the tracks. Layer by layer, a competition algorithm based on  $\chi^2$  minimization builds the tracks and assigns as many clusters as possible to them.

A generalized algorithm has been developed for the treatment of events that feature only two tracker layers with exactly three clusters. It is based on a combinatorial approach to the track finding problem and has been employed in the analysis, thus improving the lepton efficiency [6].

Subsequently, ambiguities in the x-coordinate, parallel to the magnetic field, due to the clustering in the bending plane projection only, have to be resolved. For this, a narrow corridor along the hits in the TOF system is defined, and only tracker hits within this corridor are retained. To each track, a series of helix fits is applied, taking into account each combination of hits in any of the track clusters. The final tracks are then defined by the combinations with the lowest  $\chi^2$ .

## 4.3 Vertice reconstruction

Vertex reconstruction is based on back-propagation of the tracks through the magnetic field using the functionality of the GEANT3 package [7]. The vertices of the left and right tracks are determined by parallel back-propagation from the point of the first tracker hit. The *conversion* vertex is then defined as the barycenter of the track points at the z-coordinate of closest approach of the tracks. In case the tracks intersect in the bending plane projection, the intersection point is taken as the vertex with the x-coordinate derived from geometrical interpolation.

The four-vector of the photon is reconstructed from the sum of those of the left and right track. Then, using the same algorithm as described above, the *bremsstrahlung* vertex of the photon and the middle track is computed.

No requirements are placed on the location of the bremsstrahlung vertex nor the conversion vertex.

## 4.4 Reconstruction quality and Monte Carlo

The quality of the reconstruction algorithms is verified with  $16.8 \cdot 10^6$  electron and positron events from a complete Monte Carlo simulation of the experiment using GEANT3. The momentum resolution is approximately 13 % for the downward case and 14 % for the upward case. This resolution is similar to that for single track events in the energy range of 10 GeV and above [8, 9], where our reconstruction algorithms have their peak sensitivity.

The properties of the bremsstrahlung photon can be particularly well reconstructed. The momentum resolution of the photon is 8 %, while the absolute direction error has a standard deviation of below 9 mrad.

## 5 Analysis

Analysis and suppression of background mainly rely on the evaluation of the topology and geometrical properties of the reconstructed events, and are therefore based on data from the tracker. Additionally, cuts on data from the TOF system are applied. However, substantial parts of the analysis deal with measures to account for the environmental circumstances under which the AMS-01 experiment was operated, especially the effect of the geomagnetic field.

### 5.1 Basic cuts

Several cuts have to be applied to the data in order to suppress misreconstructed events:

- Track fits with resulting momenta lower than 100 MeV/c may lead to misreconstruction. Events containing such tracks are thus rejected.
- Due to the deflection in the magnetic field, the charge signs of the secondaries are exactly constrained and depend on flight direction. The charge sum of the three tracks is required to be  $\pm 1$ .
- With higher energies, the track momentum resolution and the signal over background ratio deteriorate. Thus the total reconstructed momentum must not exceed 50 GeV/c.

The requirement for increasing cluster distances within the seed triplets along the flight path largely distinguishes between downward and upward going particles. To make sure the flight direction is correctly recognized, timing information from the TOF system is used. The time of passage in the individual scintillators is measured with a resolution of 120 ps [10]. The flight time  $t_f$  for downward and upward going particles is calculated according to  $t_f = (t_1 + t_2)/2 - t_3$ , where the  $t_i$  denote the time of passage measured in TOF layer  $i$  ( $i$  is counted from top to bottom). Due to high voltage failures in TOF layer 4 [10], its timing information is not used. The sign of  $t_f$  depends on the flight direction. Events are rejected for which  $|t_f|$  is smaller than 3.5 ns or the sign of  $t_f$  disagrees with the flight direction given by the requirement of increasing cluster distances.

To make sure that there are three particles traversing the detector, consistent with the signature of a converted bremsstrahlung photon, a minimum average energy deposition of 5 MeV (equivalent to 2 MIPs) is required in each of the last two TOF layers in the flight direction.

Nuclei such as *He* or *N* have been observed to induce background events through hadronic interactions. Such particles with  $Z > 1$  deposit significantly more energy in the subdetectors than singly charged particles. The truncated mean of the energy depositions in the TOF scintillators is calculated, and events are rejected with an energy deposition of more than 10 MeV. Additionally, a cut is applied to the mean of the three highest tracker hit amplitudes. By these means events involving nuclei are entirely eliminated.

### 5.2 Suppression of dominant background

For the suppression of background, the fact is used that bremsstrahlung and photon conversion imply small opening angles of the particles at the vertices. In order to make these angles independent of the frame of reference, the corresponding invariant masses are calculated according to

$$m_{\text{inv}}^2 = 2 \cdot E_1 \cdot E_2 \cdot (1 - \cos \theta), \quad (1)$$

where  $\theta$ ,  $E_1$  and  $E_2$  denote the opening angle and the energies of the primary particle and the photon, or the conversion pair, respectively.

The distribution of the invariant mass at the conversion vertex is shown in Figure 2. For events with negative charge, which represent a largely clean electron sample, it reveals a narrow shape with a peak at zero, in agreement with Monte Carlo results. For events with positive total charge, consisting of positrons and background, the distribution also shows a peak at zero, and an additional long tail towards higher invariant masses caused by the proton background. The distributions of the invariant mass at the bremsstrahlung vertex show similar behaviors. In order to discriminate against background events, cuts are applied on the invariant masses. The cuts are parameterized as ellipses in the invariant mass plane, centered at zero, with half axes in units of the standard deviations,  $\sigma$ , of the electron distribution from data. Events outside the ellipses are rejected. In order to keep the positron selection efficiency high, the cut values have been set to  $2\sigma$ .

### 5.3 Geomagnetic cutoff

The spectra of cosmic rays are modulated by the geomagnetic field. Depending on the incident direction and the geomagnetic coordinates of the entry point into the magnetosphere, particles with momenta below a certain cutoff are deflected by the geomagnetic field and cannot reach the Earth's proximity. Hence, below geomagnetic cutoff the particles detected by AMS-01 must originate from within the magnetosphere. They were mostly produced as secondaries through hadronic interactions and trapped on geomagnetic field lines.

To discriminate against these secondaries, particle trajectories were individually traced back from their measured incident location, angle and momentum through the geomagnetic field by numerical integration of the equation of motion [11]. A particle was rejected as a secondary if its trajectory once approached the surface of the Earth, and thus originated from an interaction with the atmosphere. Particles which did not reach a distance of 25 Earth radii were considered as trapped and also rejected.

## 6 Correction for irreducible background

As can be seen in Figure 2, the invariant mass distribution of protons does not vanish in the signal region. The same applies to the background from misidentified electrons. Consequently, a small fraction of background events will not be rejected by the cut on the invariant masses. This remaining irreducible background has to be corrected. This has been accomplished using Monte Carlo simulations.

The approach used is to run the analysis on  $16.5 \cdot 10^7$  proton and  $9.4 \cdot 10^6$  electron Monte Carlo events as if they were data, determine the momentum distribution of particles that are misidentified as positrons, and subtract these from the raw positron counts obtained from data. However, such a comparison of Monte Carlo and data requires the adjustment of several properties of the simulated events. Particularly, they have not been affected by the geomagnetic field.

As introduced in § 5.3, the geomagnetic field shields the Earth's vicinity from low energy particles. However, the geomagnetic cutoff cannot be calculated individually for Monte Carlo particles, since their four vector is not defined with respect to the geomagnetic coordinates. To correct for the shielding effect, the livetime function, described in § 8.2 is used. The livetime function gives the effective measurement time as a function of momentum for singly charged particles. Normalized to a maximum value of 1 at highest momenta well above the cutoff, its value at a given momentum denotes the probability for a particle to penetrate the geomagnetic field. Hence, it serves as a weight for distributions of any event variable from Monte Carlo, particularly for the momentum distribution

of background events from Monte Carlo. As for the data, the livetime function has to be evaluated using the reconstructed momentum, rather than the incident particle’s simulated momentum.

The incident momentum spectrum of the Monte Carlo particles follows a distribution  $\phi_{MC}(p) = p^{-1}$ , which differs significantly from the true spectrum. Since the event variables are correlated with the incident momentum, they again have to be reweighted. Using the parameterized fluxes  $\phi_D(p)$  of protons [3] and electrons [12], measured by AMS-01, the spectral reweighting function is calculated as  $w(p) = \phi_D(p)/\phi_{MC}(p)$ .

The livetime function as well as the spectral reweighting function correct for the shape of the momentum distribution of background events calculated from Monte Carlo. Subsequently, since the latter function does not conserve the integral, the background distributions need to be scaled to the data.

Figure 2b illustrates the scaling of the proton Monte Carlo to the data using the sidebands of the invariant mass distributions. The sidebands are defined as the ranges of invariant mass above certain thresholds in which the positron contribution to the sample of positively charged events from data is negligible. The thresholds are determined from the electron distribution to be  $0.16 \text{ GeV}/c^2$  at the conversion vertex and  $0.2 \text{ GeV}/c^2$  at the bremsstrahlung vertex. Below the thresholds the excess in the data due to the positron contribution is apparent.

The correction due to electrons with misreconstructed charge sign is calculated in a very similar way. The main difference is the fact that the distributions originating from a given number of Monte Carlo electrons are scaled directly to the electron candidate sample found in the data.

Using the scaling factors obtained with the above procedures, the background contribution to the number of positron candidates is calculated. Figure 3 shows the total background correction as a function of momentum, separately indicating the contributions from protons and misidentified electrons. In total, they amount to 24.9 and 6.5 events, respectively. The resulting corrected lepton sample consists of 86 positrons and 1026 electrons.

## 7 Positron fraction

The positron fraction  $e^+/(e^+ + e^-)$  is calculated from the electron counts and corrected positron counts for each energy bin. It is shown in Figure 4 in comparison with earlier results [12–14] and a model calculation based on purely secondary positron production [15]. Table 1 summarizes the results. The total errors are clearly dominated by the contribution from statistical errors, systematic errors play a lesser role. In the following, the contributions to the error on the positron fraction are discussed.

### 7.1 Statistical errors

Due to the complexity of the positron fraction computation, taking into account two sources of background, and low statistics, a Bayesian approach based on Monte Carlo simulation has been chosen for the determination of the statistical errors [16]. The aim is to acquire the probability distribution of all possible values of the positron fraction which can, superimposed on the background, lead to the observed number of particle counts. From this distribution, the confidence levels are derived by numerical integration.

In a first step, for a particular momentum bin, two random floating point numbers are generated, following a uniform distribution and representing the “true” numbers of electrons and positrons. Subsequently, the background counts from Monte Carlo – modulated with errors to account for their systematic uncertainty – are added to the true number of positrons. Here, the scale factors from background scaling have to be considered. The resulting numbers of positively and negatively charged

particles are modulated with Poisson errors, thus become integers, and then represent the “measured” number of candidates including background. If these numbers are exactly equal to the counts observed in the experiment, the positron fraction calculated from the true numbers is accepted for further analysis, and the above procedure is repeated.

The distribution of simulated positron fraction values is finally parameterized and normalized to an integral of 1. Subsequently, by repeated numerical integration, the smallest interval is found in which the integral of the distribution equals 0.683, consequently giving the lower and upper limit of the  $1\sigma$  Gaussian confidence interval.

## 7.2 Systematic errors

In the positron fraction – as a ratio of particle fluxes – most sources of systematic error, such as detector acceptance or trigger efficiency, naturally cancel out. Hence, only sources of error which are asymmetric with respect to the particle charge have to be considered.

Background correction is applied to the sample of positron candidates only and is therefore a source of systematic error. To a certain degree, the description of the experimental setup may be inaccurately implemented in the Monte Carlo program. Furthermore, in contrast to the production of charged pions, background processes involving neutral pion production imply photoconversion with typically low angles between tracks emerging from the vertices. Hence, the distribution of invariant masses depends on the cross sections of charged and neutral pion production. Possible inaccuracies in the implementation of the cross sections in the Monte Carlo program must therefore be considered.

The systematic error from background correction can be estimated by evaluating the deviation of the scaled Monte Carlo background from the data in the invariant mass plane. With a binning coarse enough to flatten statistical fluctuations, the mean deviation outside the signal region leads to a systematic error estimate of 20 % of the background events. This value is then propagated to the positron fraction for each momentum bin.

As a consequence of the East-West effect [17], in combination with the asymmetric layout of the AMS-01 tracker, the product of the detector acceptance times the livetime as functions of the particles’ incident direction may vary for positrons and electrons. Even though no deviation of their average livetimes is apparent (see § 8.2), we account for this effect with a second contribution to the systematic error of the positron fraction. It is estimated from the mean variation of the difference in livetime of positrons and electrons over the detector acceptance. After propagation to the positron fraction, the systematic error due to the East-West effect is below 10 % for all momentum bins, except for the highest momenta above 26.5 GeV, where it amounts to approximately 10 % of the positron fraction value.

## 8 Flux calculation

As a crosscheck to the measurement of the positron fraction, presented above, the absolute incident fluxes of electrons and positrons are calculated. The electron flux is then compared to measurements by other experiments and the results obtained previously by AMS-01.

One can calculate the differential flux for a given momentum bin  $p$  of width  $\Delta p$  from the measured particle count  $N(p, \theta, \phi)$  in this bin, the detector acceptance  $A(p, \theta, \phi)$ , and the livetime  $T(p, \theta, \phi)$ , as follows:

$$\frac{d\Phi(p, \theta, \phi)}{dp} = \frac{N(p, \theta, \phi)}{A(p, \theta, \phi) \cdot T(p, \theta, \phi) \cdot \Delta p} \quad (2)$$



By the term *livetime*, we mean the effective amount of time during which cosmic ray particles coming from outer space have the opportunity to reach the detector. If – as is the case with the AMS-01 downward flux – the livetime is only weakly depending on the direction, the angular distribution of the particle count will follow that of the acceptance. Then, one can approximate (2) to become

$$\frac{d\Phi(p)}{dp} = \frac{N(p)}{A(p) \cdot T(p) \cdot \Delta p}. \quad (3)$$

In the following two sections, the determination of the detector acceptance and the calculation of the livetime will be described.

## 8.1 Detector acceptance

The detector acceptance for the bremsstrahlung conversion process is calculated from Monte Carlo, separately for electrons and positrons and for downward and upward going particles. In the simulation, particles are emitted from a square surface  $S$ , with a side length of 3.9 m, above or below the detector, respectively. With  $n_t$  being the total number of Monte Carlo particles emitted from  $S$  into the hemisphere facing the detector with an isotropic angular distribution, and  $n_c$  the number of reconstructed events remaining after the cuts, the acceptance as a function of incident momentum is [18]

$$A(p) = S \cdot \pi \cdot \frac{n_c(p)}{n_t(p)}. \quad (4)$$

As Figure 5 shows,  $A(p)$  is on the order of several  $\text{cm}^2 \cdot \text{sr}$  and reaches a maximum at approximately 20 GeV/c. Towards higher momentum the decreasing cluster separation approaches the resolution limit of the silicon strip detectors, and the acceptance drops. At low momentum, by contrast, secondary particles may be deflected such that they generate multiple separated hits in the TOF scintillators. In this case events are rejected by the trigger logic of the experiment. Furthermore, the probability rises that secondary particles have a too low momentum to be properly reconstructed, hence the acceptance decreases.

Formed by the Space Shuttle’s payload bay floor and the support structure of AMS-01, additional material is traversed by upward going particles before they enter the detector, thus increasing the probability of bremsstrahlung emission and photoconversion. Consequently, the acceptance for upward going particles is generally higher with respect to downward going ones. The amount of this additional material is estimated to be 4.5 % of a radiation length. No significant difference in the acceptance for electrons and positrons is observed.

## 8.2 Calculation of livetime

Two cardinal effects can prevent cosmic ray particles from reaching the detector. First, the body of the Earth obstructs particles arriving from the “wrong” side. Second, and more complicated, the geomagnetic field forces the trajectories of incoming particles on a helix, effectively capturing particles with under-cutoff momentum. This effect depends on the position of the Space Shuttle, the incident direction and time. In addition, the periods of time during which the trigger system was busy enter as dead time into this calculation.

The livetime  $T(p)$  was derived as follows. The acceptance region of the AMS-01 detector was divided into nine bins of equal size along  $\cos(\theta)$ , in the interval of  $[0.7, 1]$ , and into eight bins along  $\phi$ . The momentum range between 1 GeV/c and 50 GeV/c was divided into eight bins. Then, for every four seconds during the flight, using the recorded position and attitude of Discovery and for each

of the 576 ( $p, d\Omega$ ) bins, a virtual charged particle was started with the corresponding values on the aperture of the detector and propagated backward through the geomagnetic field. If the virtual particle fulfilled the criteria of a primary cosmic ray particle as described in § 5.3, the interval during which the trigger was not busy was added to the total livetime.

The livetime, averaged over the detector acceptance, for downward and upward going positively and negatively charged particles, is displayed in Figure 6. Due to obstruction by the Earth, the livetime for downward going particles is twice that of upward going ones. Concerning the average livetime, no significant difference between positively and negatively charged particles is apparent.

### 8.3 Positron and electron fluxes

Since the amount of material underneath the detector is estimated only, in this analysis particle fluxes are calculated solely for particles which traverse the detector top-down. Figure 7 displays the fluxes of downward going positrons and electrons, together with results published earlier by AMS-01 [12] and HEAT- $e^\pm$  [4] with their statistical errors. The fluxes are in very good agreement with previous measurements over the full momentum range, except for a slight discrepancy in the electron fluxes between 2 and 3 GeV/c. Here, at low momentum in combination with low statistics, we expect the inaccuracies of the backtracing through the geomagnetic field to become the dominant source of systematic error to the fluxes. However, for the positron fraction as a ratio of particle counts, this effect cancels out.

## 9 Conclusions

In this paper, we present a new measurement of the cosmic ray positron fraction up to energies of 30 GeV with the AMS-01 detector. Positrons are identified by conversion of bremsstrahlung photons, which yields an overall proton rejection on the order of  $10^6$ . This approach allows to extend the energy range accessible to the experiment far beyond its design limits and to fully exhaust the detector's capabilities. The results, especially on the positron fraction, are consistent with those obtained in previous experiments at large.

For the reconstruction of converted bremsstrahlung events, customized algorithms for track finding and event reconstruction have been developed and implemented. We have shown that the background is controllable and the overall uncertainty is dominated by the statistical error due to the low overall cross section of the signal process.

Furthermore, the absolute lepton fluxes have been calculated and found to match the earlier results. This required a new precise and extensive livetime calculation.

## Acknowledgments

The support of INFN, Italy, ETH–Zürich, the University of Geneva, the Chinese Academy of Sciences, Academia Sinica and National Central University, Taiwan, the RWTH–Aachen, Germany, the University of Turku, the University of Technology of Helsinki, Finland, the U.S. DOE and M.I.T., CIEMAT, Spain, LIP, Portugal and IN2P3, France, is gratefully acknowledged.

The success of the first AMS mission is due to many individuals and organizations outside of the collaboration. The support of NASA was vital in the inception, development and operation of the experiment. Support from the Max–Planck Institute for Extraterrestrial Physics, from the space agencies of Germany (DLR), Italy (ASI), France (CNES) and China and from CSIST, Taiwan also played important roles in the success of AMS.

## References

- [1] S. Eidelmann et al., Phys. Lett. B **592** (2004) 206
- [2] M. Turner, F. Wilczek, Phys. Rev. D **42** (1990) 1001
- [3] M. Aguilar et al., Phys. Rep. **366** (2002) 331
- [4] M. A. DuVernois et al., ApJ **559** (2001) 296
- [5] J. Olzem, PhD thesis in preparation, RWTH Aachen (2007)
- [6] H. Gast, Diploma thesis, RWTH Aachen (2004)
- [7] R. Brun et al., CERN DD/EE/84-1 (1987)
- [8] J. Alcaraz et al., Nuov. Cim. A **112** (1999) 1325
- [9] Y.-H. Chang, Nucl. Instrum. Meth. A **466** (2001) 282
- [10] D. Alvisi et al., Nucl. Instrum. Meth. A **437** (1999) 212
- [11] E. Flückiger, E. Kobel, J. Geomag. Geoelectr. **42** (1990) 1123
- [12] J. Alcaraz et al., Phys. Lett. B **484** (2000) 10
- [13] R. L. Golden et al., ApJ **457** (1996) L103
- [14] J. J. Beatty et al., Phys. Rev. Lett. **93** (2004) 241102
- [15] I. V. Moskalenko, A. W. Strong, ApJ **493** (1998) 694
- [16] O. Helene, Nucl. Instrum. Meth. **212** (1983) 319;  
O. Helene, Nucl. Instrum. Meth. A **228** (1984) 120
- [17] T. Johnson, Phys. Rev. **45** (1934) 569
- [18] J. D. Sullivan, Nucl. Instrum. Meth. **95** (1971) 5

# The AMS–01 Collaboration

M. Aguilar,<sup>z</sup> J. Alcaraz,<sup>z</sup> J. Allaby,<sup>r</sup> B. Alpat,<sup>ad</sup> G. Ambrosi,<sup>ad</sup> H. Anderhub,<sup>ai</sup> L. Ao,<sup>g</sup> A. Arefiev,<sup>ac</sup> P. Azzarello,<sup>ad</sup> L. Baldini,<sup>j,l</sup> M. Basile,<sup>j</sup> D. Barancourt,<sup>t</sup> F. Barao,<sup>x,w</sup> G. Barbier,<sup>t</sup> G. Barreira,<sup>x</sup> R. Battiston,<sup>ad</sup> R. Becker,<sup>l</sup> U. Becker,<sup>l</sup> L. Bellagamba,<sup>j</sup> P. Béné,<sup>s</sup> J. Berdugo,<sup>z</sup> P. Berges,<sup>l</sup> B. Bertucci,<sup>ad</sup> A. Biland,<sup>ai</sup> S. Blasko,<sup>ad</sup> G. Boella,<sup>aa</sup> M. Boschini,<sup>aa</sup> M. Bourquin,<sup>s</sup> L. Brocco,<sup>j</sup> G. Bruni,<sup>j</sup> M. Buénerd,<sup>t</sup> J. D. Burger,<sup>l</sup> W. J. Burger,<sup>ad</sup> X. D. Cai,<sup>l</sup> C. Camps,<sup>b</sup> P. Cannarsa,<sup>ai</sup> M. Capell,<sup>l</sup> F. Cardano,<sup>ad</sup> D. Casadei,<sup>j</sup> J. Casaus,<sup>z</sup> G. Castellini,<sup>p,j</sup> Y. H. Chang,<sup>m</sup> H. F. Chen,<sup>u</sup> H. S. Chen,<sup>i</sup> Z. G. Chen,<sup>g</sup> N. A. Chernoplekov,<sup>ab</sup> T. H. Chiueh,<sup>m</sup> K. Cho,<sup>o</sup> M. J. Choi,<sup>af</sup> Y. Y. Choi,<sup>af</sup> F. Cindolo,<sup>j</sup> V. Commichau,<sup>b</sup> A. Contin,<sup>j</sup> E. Cortina-Gil,<sup>s</sup> M. Cristinziani,<sup>s</sup> T. S. Dai,<sup>l</sup> C. Delgado,<sup>z</sup> S. Difalco,<sup>ae</sup> L. Djambazov,<sup>ai</sup> I. D'Antone,<sup>j</sup> Z. R. Dong,<sup>h</sup> P. Emonet,<sup>s</sup> J. Engelberg,<sup>v</sup> F. J. Eppling,<sup>l</sup> T. Eronen,<sup>ah</sup> G. Esposito,<sup>ad</sup> P. Extermann,<sup>s</sup> J. Favier,<sup>c</sup> E. Fiandrini,<sup>ad</sup> P. H. Fisher,<sup>l</sup> G. Flügge,<sup>b</sup> N. Fouque,<sup>c</sup> Yu. Galaktionov,<sup>ac,l</sup> H. Gast,<sup>a</sup> M. Gervasi,<sup>aa</sup> P. Giusti,<sup>j</sup> D. Grandi,<sup>aa</sup> O. Grimm,<sup>ai</sup> W. Q. Gu,<sup>h</sup> K. Hangarter,<sup>b</sup> A. Hasan,<sup>ai</sup> V. Hermel,<sup>c</sup> H. Hofer,<sup>ai</sup> W. Hungerford,<sup>ai</sup> M. Jongmanns,<sup>ai</sup> K. Karlamaa,<sup>v</sup> W. Karpinski,<sup>a</sup> G. Kenney,<sup>ai</sup> D. H. Kim,<sup>o</sup> G. N. Kim,<sup>o</sup> K. S. Kim,<sup>af</sup> M. Y. Kim,<sup>af</sup> A. Klimentov,<sup>l,ac</sup> R. Kossakowski,<sup>c</sup> A. Kounine,<sup>l</sup> V. Koutsenko,<sup>l,ac</sup> M. Kraeber,<sup>ai</sup> G. Laborie,<sup>t</sup> T. Laitinen,<sup>ah</sup> G. Lamanna,<sup>ad,1</sup> E. Lanciotti,<sup>z</sup> G. Laurenti,<sup>j</sup> A. Lebedev,<sup>l</sup> C. Lechanoine-Leluc,<sup>s</sup> M. W. Lee,<sup>o</sup> S. C. Lee,<sup>ag</sup> G. Levi,<sup>j</sup> C. L. Liu,<sup>y</sup> H. T. Liu,<sup>j</sup> G. Lu,<sup>g</sup> Y. S. Lu,<sup>j</sup> K. Lübelmeyer,<sup>a</sup> D. Luckey,<sup>l</sup> W. Lustermaun,<sup>ai</sup> C. Mañá,<sup>z</sup> A. Margotti,<sup>j</sup> F. Mayet,<sup>t</sup> R. R. McNeil,<sup>e</sup> B. Meillon,<sup>t</sup> M. Menichelli,<sup>ad</sup> A. Mihul,<sup>k</sup> A. Mujunen,<sup>v</sup> A. Oliva,<sup>ad</sup> J. Olzem,<sup>a</sup> F. Palmonari,<sup>j</sup> H. B. Park,<sup>o</sup> W. H. Park,<sup>o</sup> M. Pauluzzi,<sup>ad</sup> F. Pauss,<sup>ai</sup> E. Perrin,<sup>s</sup> A. Pesci,<sup>j</sup> A. Pevsner,<sup>d</sup> F. Pilo,<sup>ae</sup> M. Pimenta,<sup>x,w</sup> V. Plyaskin,<sup>ac</sup> V. Pojidaev,<sup>ac</sup> M. Pohl,<sup>s</sup> N. Produit,<sup>s</sup> P. G. Rancoita,<sup>aa</sup> D. Rapin,<sup>s</sup> F. Raupach,<sup>a</sup> D. Ren,<sup>ai</sup> Z. Ren,<sup>ag</sup> M. Ribordy,<sup>s</sup> J. P. Richeux,<sup>s</sup> E. Riihonen,<sup>ah</sup> J. Ritakari,<sup>v</sup> S. Ro,<sup>o</sup> U. Roeser,<sup>ai</sup> C. Rossin,<sup>t</sup> R. Sagdeev,<sup>n</sup> D. Santos,<sup>t</sup> G. Sartorelli,<sup>j</sup> C. Sbarra,<sup>j</sup> S. Schael,<sup>a</sup> A. Schultz von Dratzig,<sup>a</sup> G. Schwering,<sup>a</sup> E. S. Seo,<sup>n</sup> J. W. Shin,<sup>o</sup> E. Shoumilov,<sup>ac</sup> V. Shoutko,<sup>l</sup> T. Siedenburger,<sup>l</sup> R. Siedling,<sup>a</sup> D. Son,<sup>o</sup> T. Song,<sup>h</sup> F. Spinella,<sup>ae</sup> M. Steuer,<sup>l</sup> G. S. Sun,<sup>h</sup> H. Suter,<sup>ai</sup> X. W. Tang,<sup>i</sup> Samuel C. C. Ting,<sup>l</sup> S. M. Ting,<sup>l</sup> M. Tornikoski,<sup>v</sup> J. Torsti,<sup>ah</sup> J. Trümper,<sup>q</sup> J. Ulbricht,<sup>ai</sup> S. Urpo,<sup>v</sup> E. Valtonen,<sup>ah</sup> J. Vandenhirtz,<sup>a</sup> E. Velikhov,<sup>ab</sup> B. Verlaat,<sup>ai,2</sup> I. Vetlitsky,<sup>ac</sup> F. Vezzu,<sup>t</sup> J. P. Vialle,<sup>c</sup> G. Viertel,<sup>ai</sup> D. Vité,<sup>s</sup> H. Von Gunten,<sup>ai</sup> S. Waldmeier Wicki,<sup>ai</sup> W. Wallraff,<sup>a</sup> B. C. Wang,<sup>y</sup> J. Z. Wang,<sup>g</sup> K. Wiik,<sup>v</sup> C. Williams,<sup>j</sup> S. X. Wu,<sup>l,m</sup> P. C. Xia,<sup>h</sup> S. Xu,<sup>l</sup> J. L. Yan,<sup>g</sup> L. G. Yan,<sup>h</sup> C. G. Yang,<sup>i</sup> J. Yang,<sup>af</sup> M. Yang,<sup>i</sup> S. W. Ye,<sup>u,3</sup> Z. Z. Xu,<sup>u</sup> H. Y. Zhang,<sup>f</sup> Z. P. Zhang,<sup>u</sup> D. X. Zhao,<sup>h</sup> Y. Zhou,<sup>ag</sup> G. Y. Zhu,<sup>i</sup> W. Z. Zhu,<sup>g</sup> H. L. Zhuang,<sup>i</sup> A. Zichichi,<sup>j</sup> B. Zimmermann,<sup>ai</sup> P. Zuccon.<sup>ad</sup>

---

<sup>a</sup> I. Physikalisches Institut, RWTH, D-52074 Aachen, Germany<sup>4</sup>

<sup>b</sup> III. Physikalisches Institut, RWTH, D-52074 Aachen, Germany<sup>4</sup>

<sup>c</sup> LAPP, Université de Savoie, CNRS/IN2P3, F-74941 Annecy-le-Vieux Cedex, France

<sup>d</sup> Johns Hopkins University, Baltimore, MD 21218, USA

<sup>e</sup> Louisiana State University, Baton Rouge, LA 70803, USA

<sup>f</sup> Center of Space Science and Application, Chinese Academy of Sciences, 100080 Beijing, China

<sup>g</sup> Chinese Academy of Launching Vehicle Technology, CALT, 100076 Beijing, China

<sup>h</sup> Institute of Electrical Engineering, IEE, Chinese Academy of Sciences, 100080 Beijing, China

<sup>i</sup> Institute of High Energy Physics, IHEP, Chinese Academy of Sciences, 100039 Beijing, China<sup>5</sup>

<sup>j</sup> University of Bologna and INFN-Sezione di Bologna, I-40126 Bologna, Italy<sup>6</sup>

<sup>k</sup> Institute of Microtechnology, Politechnica University of Bucharest and University of Bucharest, R-76900 Bucharest, Romania

<sup>l</sup> Massachusetts Institute of Technology, Cambridge, MA 02139, USA

<sup>m</sup> National Central University, Chung-Li, Taiwan 32054

<sup>n</sup> University of Maryland, College Park, MD 20742, USA

<sup>o</sup> CHEP, Kyungpook National University, 702-701 Daegu, Korea

- <sup>p</sup> CNR–IROE, I-50125 Florence, Italy
- <sup>q</sup> Max–Planck Institut für extraterrestrische Physik, D-85740 Garching, Germany
- <sup>r</sup> European Laboratory for Particle Physics, CERN, CH-1211 Geneva 23, Switzerland
- <sup>s</sup> University of Geneva, CH-1211 Geneva 4, Switzerland
- <sup>t</sup> Laboratoire de Physique Subatomique et de Cosmologie, IN2P3/CNRS, F-38026 Grenoble, France
- <sup>u</sup> Chinese University of Science and Technology, USTC, Hefei, Anhui 230 029, China<sup>5</sup>
- <sup>v</sup> Helsinki University of Technology, FIN-02540 Kylmala, Finland
- <sup>w</sup> Instituto Superior Técnico, IST, P-1096 Lisboa, Portugal
- <sup>x</sup> Laboratório de Instrumentação e Física Experimental de Partículas, LIP, P-1000 Lisboa, Portugal
- <sup>y</sup> Chung–Shan Institute of Science and Technology, Lung-Tan, Tao Yuan 325, Taiwan
- <sup>z</sup> Centro de Investigaciones Energéticas, Medioambientales y Tecnológicas, CIEMAT, E-28040 Madrid, Spain<sup>7</sup>
- <sup>aa</sup> INFN-Sezione di Milano, I-20133 Milan, Italy<sup>6</sup>
- <sup>ab</sup> Kurchatov Institute, Moscow, 123182 Russia
- <sup>ac</sup> Institute of Theoretical and Experimental Physics, ITEP, Moscow, 117259 Russia
- <sup>ad</sup> INFN-Sezione di Perugia and Università Degli Studi di Perugia, I-06100 Perugia, Italy<sup>6</sup>
- <sup>ae</sup> INFN-Sezione di Pisa and Università di Pisa, I-56100 Pisa, Italy<sup>6</sup>
- <sup>af</sup> Ewha Womens University, 120-750 Seoul, Korea
- <sup>ag</sup> Institute of Physics, Academia Sinica, Nankang Taipei 11529, Taiwan
- <sup>ah</sup> University of Turku, FIN-20014 Turku, Finland
- <sup>ai</sup> Eidgenössische Technische Hochschule, ETH Zürich, CH-8093 Zürich, Switzerland
- <sup>1</sup> Present address: LAPP, Université de Savoie, CNRS/IN2P3, F-74941 Annecy-le-Vieux Cedex, France
- <sup>2</sup> Now at National Institute for High Energy Physics, NIKHEF, NL-1009 DB Amsterdam, The Netherlands.
- <sup>3</sup> Supported by ETH Zürich.
- <sup>4</sup> Supported by the Deutsches Zentrum für Luft– und Raumfahrt, DLR.
- <sup>5</sup> Supported by the National Natural Science Foundation of China.
- <sup>6</sup> Also supported by the Italian Space Agency.
- <sup>7</sup> Also supported by the Comisión Interministerial de Ciencia y Tecnología.

Momentum [GeV/c]	$N_{e^-}$	$N_{e^+}$	Positron fraction	$\sigma_{\text{stat}}$	$\sigma_{\text{sys,b}}$	$\sigma_{\text{sys,l}}$
1.0– 1.5	11	3.0	0.210	+0.11 -0.1	$\pm 0$	$\pm 0$
1.5– 2.0	31	4.8	0.133	+0.064 -0.051	+0.002 -0	$\pm 0.006$
2.0– 3.0	85	10.7	0.112	+0.034 -0.031	+0.001 -0.003	$\pm 0.004$
3.0– 4.5	186	15.8	0.078	+0.021 -0.018	+0.001 -0.003	$\pm 0.004$
4.5– 6.0	172	10.0	0.055	+0.025 -0.022	+0.006 -0.007	$\pm 0.001$
6.0– 8.9	198	9.0	0.043	+0.029 -0.017	+0.01 -0.004	$\pm 0.004$
8.9– 14.8	195	14.5	0.069	+0.03 -0.014	+0.01 -0.002	$\pm 0.006$
14.8– 26.5	109	15.4	0.124	+0.038 -0.03	+0.009 -0.003	$\pm 0.007$
26.5– 50.0	39	2.9	0.070	+0.075 -0.034	+0.01 -0.01	$\pm 0.007$

Table 1: The number of electron ( $N_{e^-}$ ) and corrected positron ( $N_{e^+}$ ) candidates and the positron fraction as a function of momentum. Systematic errors are given separately for background ( $\sigma_{\text{sys,b}}$ ) and livetime ( $\sigma_{\text{sys,l}}$ ) correction.

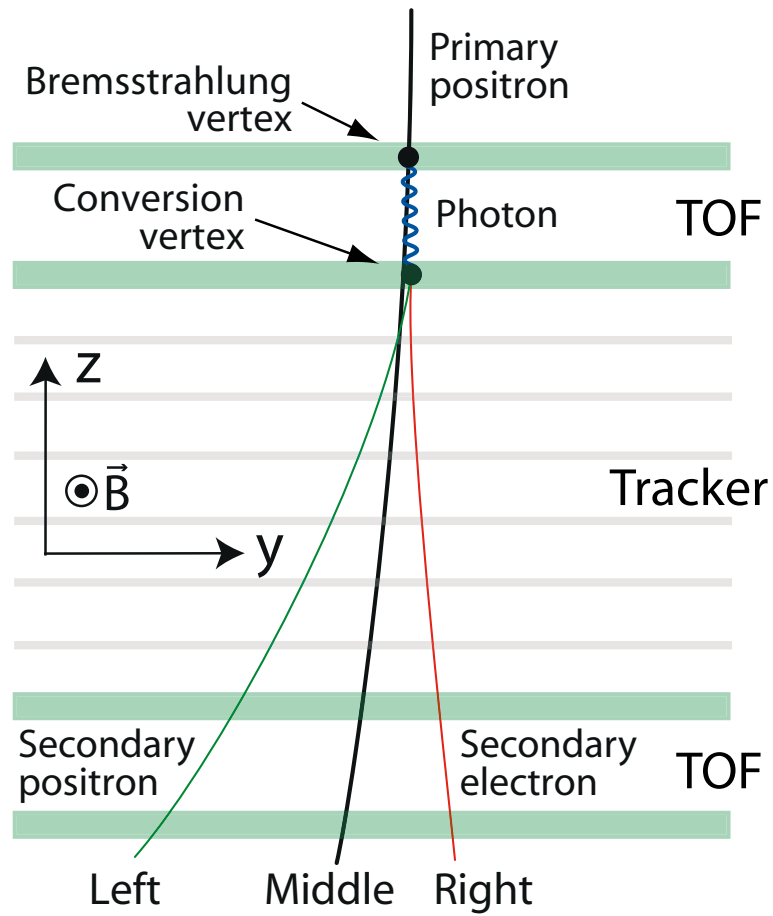


Figure 1: Schematic view of a converted bremsstrahlung event caused by a positron going top-down.

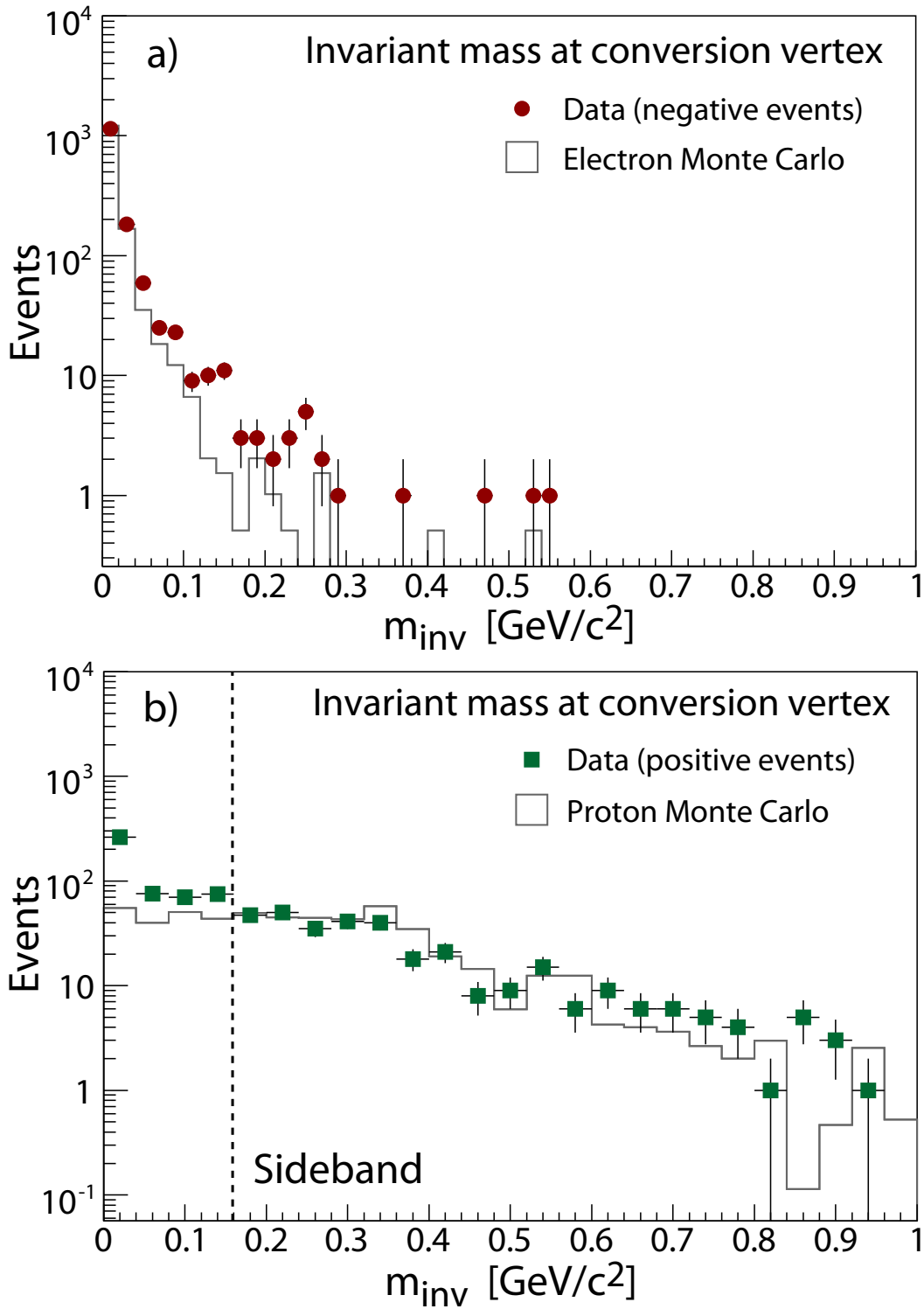


Figure 2: a) Invariant mass distribution at the conversion vertex for negatively charged data events (circles) and electron Monte Carlo (histogram). b) The same display for positively charged data events (squares) and proton Monte Carlo (histogram). The proton Monte Carlo distribution has been scaled to the data using the sideband. Below the sideband threshold of  $0.16 \text{ GeV}/c^2$ , the excess in the data due to the positron contribution is apparent.



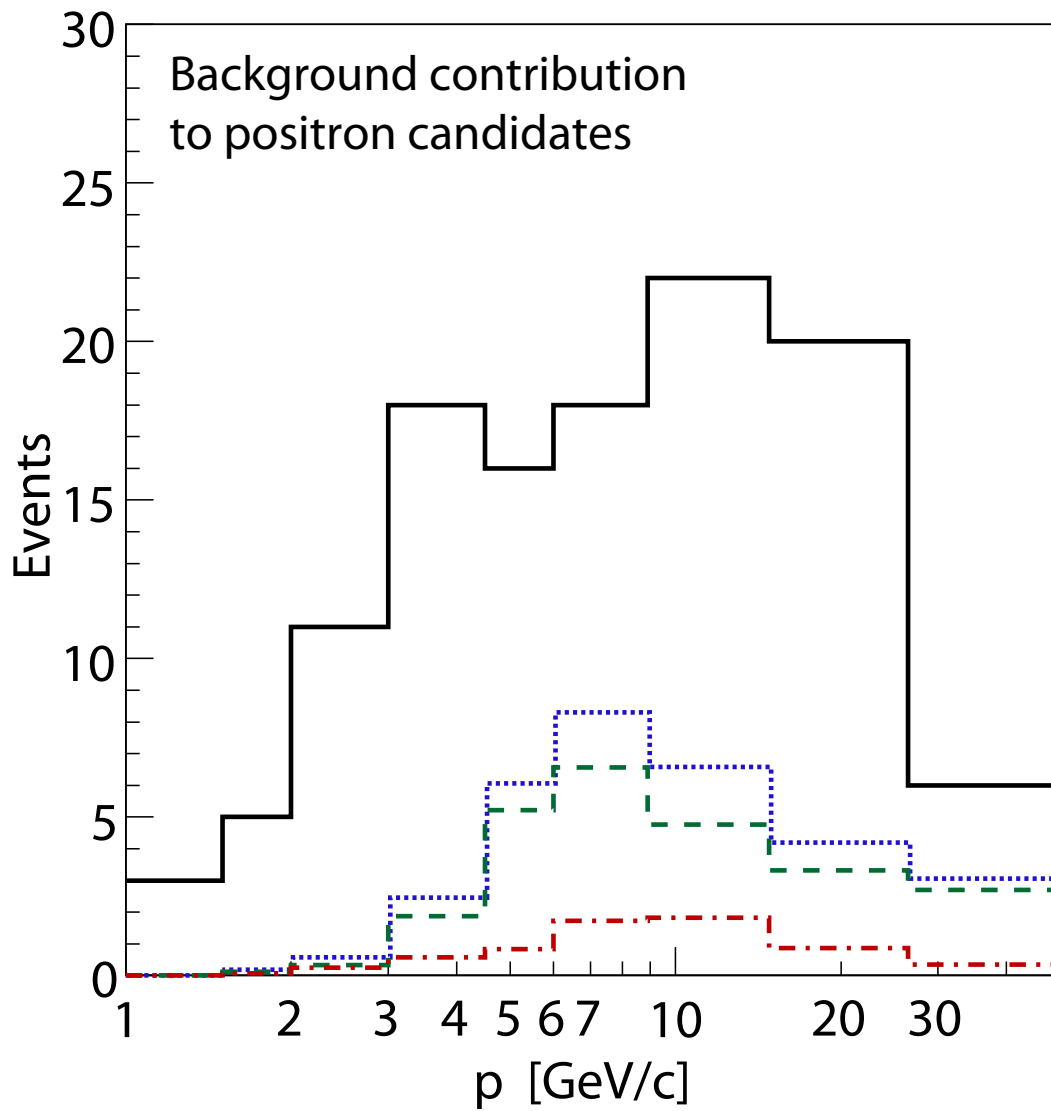


Figure 3: Momentum distribution of the positron candidates including background (solid line) and the total estimated background (blue dotted line), itemized into contributions from protons (green dashed line) and wrongly identified electrons (red dash-dotted line).

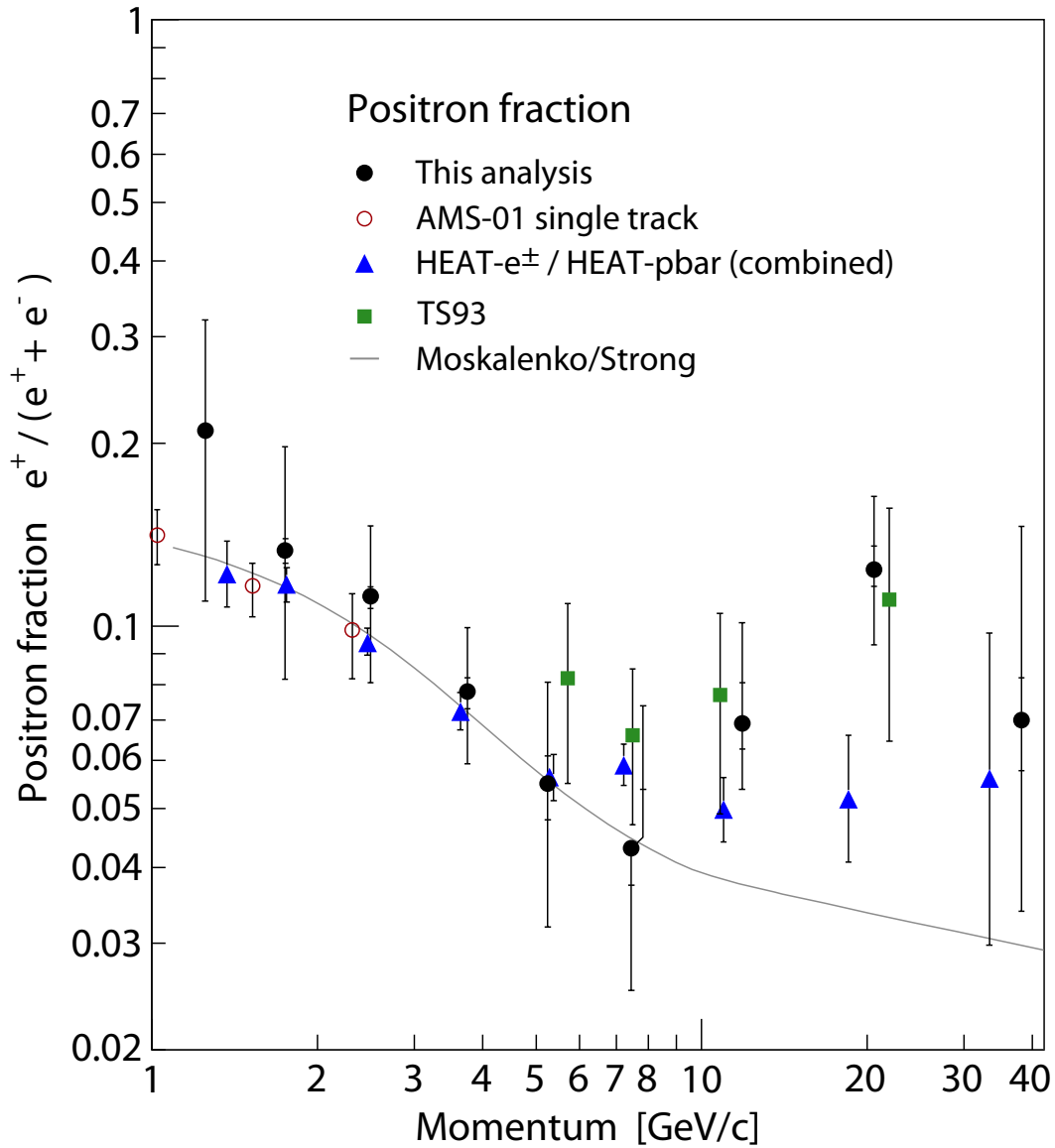


Figure 4: The positron fraction  $e^+/(e^+ + e^-)$  measured in this analysis (filled circles), compared with earlier results from AMS-01 (open circles) [12], TS93 (squares) [13], the combined results from HEAT- $e^\pm$  and HEAT-pbar (triangles) [14], together with a model calculation for purely secondary positron production from [15] (solid line). The total error is given by the outer error bars, while the inner bars represent the systematic contribution to the total error.

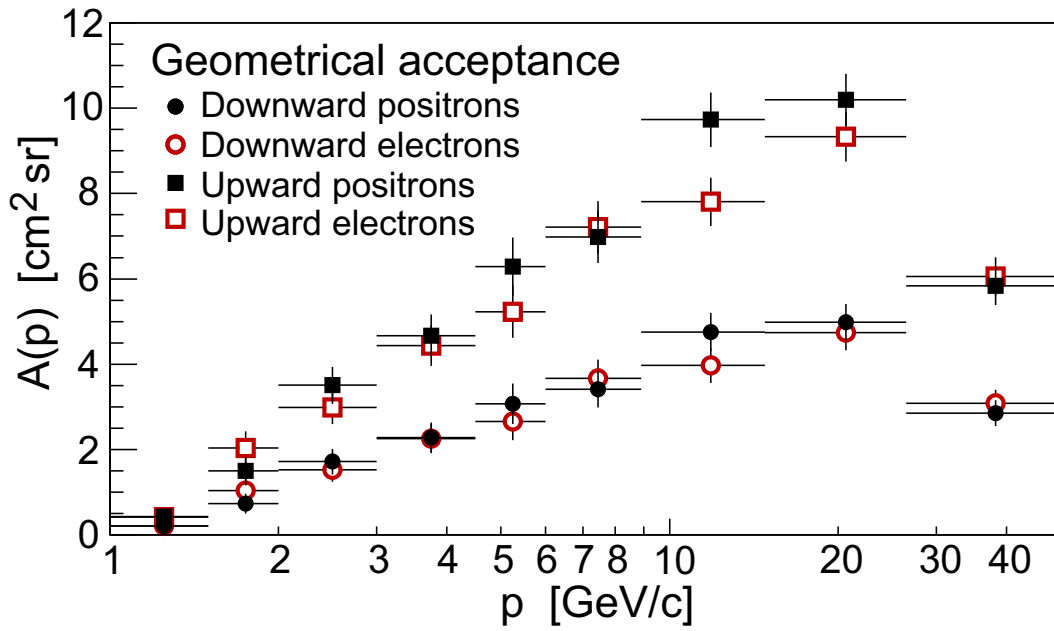


Figure 5: The geometrical acceptance for downward (circles) and upward (squares) going positrons (filled) and electrons (open), when identified through bremsstrahlung conversion.

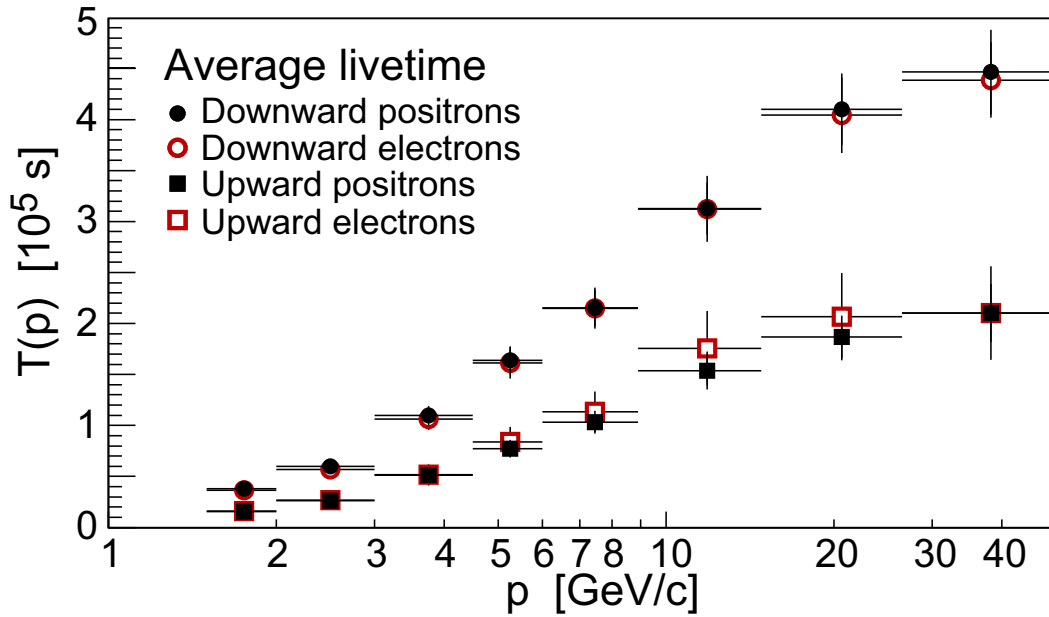


Figure 6: The livetimes, averaged over the detector acceptance, as functions of momentum for downward (circles) and upward (squares) going positrons (filled) and electrons (open).

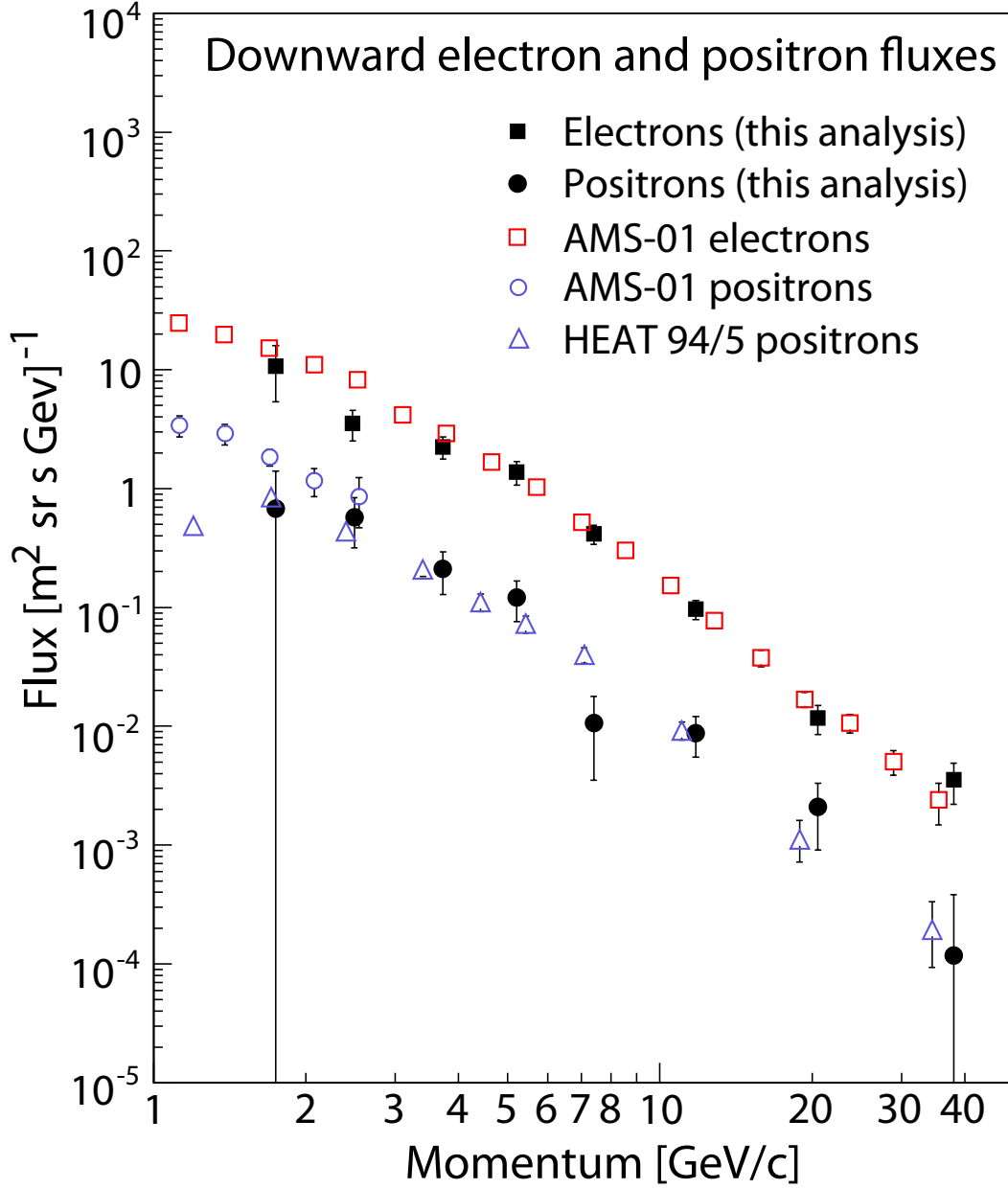


Figure 7: The fluxes of downward going positrons (filled circles) and electrons (filled squares) measured in this analysis, compared with earlier results from AMS-01 (open circles and squares) [12] and HEAT- $e^\pm$  (triangles) [4]. Error bars denote statistical errors only.